Nonreciprocal Weyl semimetal waveguide

Marco Peluso ◉,[1] Alessandro De Martino ◉,[2] Reinhold Egger ◉,[3] and Francesco Buccheri ◉[1,4]

[1]*Dipartimento di Scienza Applicata e Tecnologia, Politecnico di Torino, Corso Duca degli Abruzzi 24, 10129 Torino, Italy*
[2]*Department of Mathematics, City St George's, University of London, Northampton Square, EC1V OHB London, United Kingdom*
[3]*Institut für Theoretische Physik, Heinrich-Heine-Universität, D-40225 Düsseldorf, Germany*
[4]*INFN Sezione di Torino, Via P. Giuria 1, 10125 Torino, Italy*

We study a cylindrical plasmonic waveguide consisting of a magnetic Weyl semimetal embedded in a dielectric medium. We determine the dispersion relation of the surface plasmon polaritons and show how it depends on the plasma frequency, the radius of the semimetal core, and the separation between the nodes. We show that the band structure, which modifies the electrodynamics in the medium, manifests itself through a pronounced asymmetry in the dispersion curves and a giant splitting in the group velocity, with the orbital angular momentum as a control parameter for the direction of propagation.

I. INTRODUCTION

Surface plasmon polaritons (SPPs) are coherent excitations of electrons and radiation, confined at the interface between a metal and a dielectric. The possibility of confining the radiation on subwavelength scales allows us to greatly enhance the intensity of the electromagnetic field and its interaction with matter [1]. A plasmonic waveguide, in particular, exploits the SPPs to overcome the limitations in light confinement caused by diffraction and to reduce the size of the device, which can reach diameters down to tens of nm [2,3]. It is also the basic component of a number of devices, e.g., SPP nanolasers [2,4]. Controlling the direction of SPPs is often necessary to reduce noise and desirable for various applications, e.g., circulators or amplifiers [5]. It requires, however, specially engineered circuit elements [6,7] or interfaces [8].

In this work, we explore the possibility of using a Weyl semimetal (WS) as constituent element of the waveguide. WSs are topological materials, exhibiting nondegenerate band touching points in an otherwise gapped Brillouin zone [9]. Since their discovery [10,11], a large number of compounds have been shown to exhibit a WS phase [12–14], eliciting intense theoretical and experimental interest. These materials possess nontrivial transport properties [15,16], which can be traced back to the presence of an axionic term in the emergent electrodynamics [17,18], directly connected to a chiral anomaly [19]. In our approach, we exploit these features to propose a novel way to control the propagation of plasmonic excitations. More in detail, the axionic term in a WS is quasi-universal, in that it is fully determined by universal constants, while the realization-specific structure of the electronic band

only enters via the separation of the band-touching points. This term encodes the anomalous Hall effect, the chiral magnetic response [20–22], and the optical activity [23,24]. The giant nonreciprocity in magnetic WSs results in significant magneto-optical effects, which can be exploited to design plasmonic circuit elements, e.g., subwavelength optical insulators [25].

At planar interfaces between WSs and dielectrics, unique properties of the SPPs emerge from the strong coupling between light and the chiral surface Fermi arcs [26,27]. As a consequence, SPPs exhibit an anisotropic dispersion in a half-space geometry [28–30]. Analogously, the optical response of thin films [31], hybrid layered structures [32,33], and magnetic domain interfaces [34,35] exhibits a strongly anisotropic character [36]. Despite its potential technological impact, a WS waveguide with a compact transverse section has not yet been studied. Importantly, a compact section allows a previously overlooked effect, namely the nonreciprocity of light propagation with respect to the orbital angular momentum (OAM) quantum number.

To show this, we investigate a one-dimensional waveguide with a circular section, in which a dielectric coating surrounds a topological magnetic WS cylindrical wire, with the magnetization along the axis. This design exploits the fact that only a portion of the energy is carried in the dissipative medium, so that long-range SPPs are supported. In addition, the reduced density of states and the electronic band structure enhance the propagation of the electromagnetic field in this class of materials [37]. Light beams can be characterized by a polarization, or by an OAM index [38]. Such Laguerre-Gaussian beams can be generated with a high degree of control [39]. In this work, we show that the interplay between the transverse confinement in the WS wire and the axionic term determines a novel nonreciprocity of the dispersion in the OAM. Remarkably, plasmons with OAM equal in modulus but opposite in sign propagate with a different, and in some regimes opposite, group velocity. This previously overlooked phenomenon can
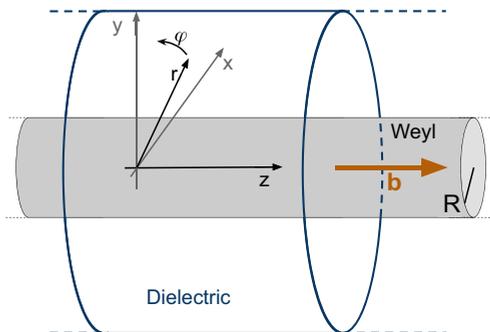
FIG. 1. Cylindrical waveguide scheme: a magnetic WS core surrounded by a dielectric medium. The wave vector **b** along the z direction describes the Weyl node separation in momentum space.

be exploited to control the signal propagation within the Weyl semimetal plasmonic waveguide (WPW), providing an additional degree of freedom to the bands available for energy and information transport [40,41].

II. MODEL

We consider a magnetic WS with a single pair of band crossings, or Weyl nodes. Such a phase has been predicted in various materials, e.g., $EuCd_2As_2$ [42–44], $HgCr_2Se_4$ [45], $MnBi_2Te_4$ [46], $MnSn_2Sb_2Te_6$ [47,48], $K_2Mn_3(AsO_4)_3$, $XCrTe$ (X = K,Rb) [49], and $Eu_2Ir_2O_7$ [50], and manufacturing Weyl semimetal nanowires is within present-day capabilities [51]. The universal low-energy Hamiltonian describing the electron dynamics in the vicinity of a Weyl node at $\mathbf{k} = \pm\mathbf{b}$ is given by

$$H_\chi(\mathbf{k}) = \hbar v_F \boldsymbol{\sigma} \cdot (\mathbf{k} - \chi\mathbf{b}), \quad \chi = \pm, \tag{1}$$

where $\boldsymbol{\sigma} = (\sigma^x, \sigma^y, \sigma^z)$ are the Pauli matrices, $\mathbf{k}$ is the electronic crystal momentum, and v_F is the Fermi velocity, typically of order $\sim 10^5$ m/s. We denote the vector that separates the Weyl nodes as $2\mathbf{b}$ and set its orientation along the k_z axis. A cylinder of radius R, with its axis along the z direction, is considered; see Fig. 1. The semimetal is surrounded by a cylindrical dielectric, with relative permittivity ϵ_d approximately independent of radiation frequency and wave vector. As we are interested in modes whose intensity decays radially in the dielectric, we assume that the outer diameter of the coating is much larger than all the other length scales.

The electronic states in this configuration have been studied in [52–55], but we will describe the SPPs via a different approach, using the dynamics of the electromagnetic field. When coupled to the Weyl electrons, the dynamics can be reformulated in terms of a Dirac action; in doing so, the electromagnetic part of the action acquires an additional term, proportional to the chiral anomaly [20–22,56,57]. Such a θ term is universal, i.e., independent of the realization of the WS phase up to the separation between the Weyl nodes in the Brillouin zone, and so are its observable consequences, e.g., the anomalous Hall and the chiral magnetic effects. It follows that, neglecting the possible shift in energy between the Weyl

nodes, the classical dynamics of the electromagnetic field is governed by the axion electrodynamics equations [17,58]

$$\nabla \cdot \mathbf{E} = \frac{\rho_e}{\varepsilon_0} + \frac{2\alpha c}{\pi}\mathbf{b} \cdot \mathbf{B}, \tag{2}$$

$$\nabla \times \mathbf{E} = -\partial_t \mathbf{B}, \tag{3}$$

$$\nabla \cdot \mathbf{B} = 0, \tag{4}$$

$$\nabla \times \mathbf{B} = \frac{1}{c^2}\partial_t \mathbf{E} + \mu_0 \mathbf{j}_e - \frac{2\alpha}{\pi c}\mathbf{b} \times \mathbf{E}. \tag{5}$$

Here $\alpha = e^2/4\pi\varepsilon_0\hbar c \approx 1/137$ is the fine-structure constant, ρ_e and $\mathbf{j}_e$ are the total charge and current densities, while ε_0 is the permittivity of the vacuum. While the homogeneous equations (3) and (4) are unaltered, the Weyl node separation $2\mathbf{b}$ explicitly appears in the anomalous density in (2) and in the Ampère-Maxwell law (5). These anomalous terms break time-reversal invariance of Maxwell's equations. Throughout this paper, we consider a monochromatic mode of angular frequency ω, $\mathbf{E}(t, \mathbf{r}) = e^{-i\omega t}\mathbf{E}(\mathbf{r})$, where $\mathbf{E}(\mathbf{r})$ is the complex field amplitude, and we omit the frequency argument.

The interaction of light with the electrons in the semimetal elicits a current density $\mathbf{j}_e = [\sigma - i\omega\varepsilon_0(\epsilon_W - 1)]\mathbf{E}$. Here, $\sigma(\omega)$ is the dynamical conductivity of a Dirac semimetal in the long-wavelength limit, and ϵ_W is the static background relative dielectric constant. While the conductivity σ is diagonal, the vector $\mathbf{b}$ generates the off-diagonal terms, see (5), which produce the quasiuniversal anomalous Hall effect [20,59]. The electronic matter determines the functional form of the relative permittivity $\mathcal{E}(\omega) = \epsilon_W + i\sigma(\omega)/\varepsilon_0\omega$ [60]. In the local-response and low-temperature approximations, it takes the form [30,61]

$$\mathcal{E} = \epsilon_W\left(1 - \frac{\omega_p^2}{\omega^2}\right) + \frac{\omega_p^2}{4\omega_F^2}\left[\ln\frac{4\omega_c^2}{|\omega^2 - 4\omega_F^2|} + i\pi\Theta(\omega - 2\omega_F)\right], \tag{6}$$

where finite lifetime effects are neglected. Here $\omega_p^2 = e^2\omega_F^2/3\pi^2\epsilon_W\varepsilon_0\hbar v_F$ denotes the squared plasma frequency in the Drude-like (or single-band) approximation, in which one retains only the first term in Eq. (6). $E_F = \hbar\omega_F$ is the Fermi energy, and $E_c = \hbar\omega_c$ is a cutoff energy, determined by the range of energies in which a linear behavior is a good description of the electronic spectrum [23], and transitions to other bands can be excluded. While the plasma frequency is properly defined as the zero of the real part of (6), ω_p is a very good approximation for realistic values of the cutoff and Fermi energies. Interestingly, ω_p can be comparable to ω_F.

There are three relevant frequency scales. The plasma frequency ω_p and the frequency cb associated with the separation between the Weyl nodes are characteristic of the bulk. The finite section introduces the scale c/R, associated with the transverse size. The dispersions of the electromagnetic field eigenmodes depend on the two dimensionless combinations

$$\rho = \frac{\omega_p R}{c}, \qquad \beta = \frac{\alpha cb}{\pi\omega_p}, \tag{7}$$

which parametrize the radius of the inner cylinder of the WPW and the separation between the Weyl nodes.

III. SPP MODES

We now proceed to calculate the normal modes of the modified Maxwell electrodynamics. We first solve the wave equation in the bulk; then, we determine the dispersion relation of the SPPs by imposing the appropriate matching conditions for the fields at the interface between the WS and the dielectric. We focus throughout on modes decaying on both sides of the interface.

The solution of Eqs. (2)–(5) in the frequency domain exploits the cylindrical symmetry of the system. In cylindrical coordinates (r, φ, z), one writes the electric field in the form

$$\mathbf{E}(r, \varphi, z) = \sum_m e^{iq_z z + im\varphi} \mathbf{E}_m(r), \qquad (8)$$

where q_z is the wave vector along the axis, and $m \in \mathbb{Z}$ is the OAM label. The vector field $\mathbf{E}_m(r)$ is further constrained by the cylindrical symmetry; see Appendix A. There, we show that the dispersion relation is determined by seeking a solution in the form (8) and subsequently imposing the consistency of the axion electrodynamics equations. The presence of the extra term in the nonhomogeneous Maxwell equations modifies the dispersion relation of the electromagnetic modes in the bulk of the material. The latter is implicitly determined by the equation

$$(\omega^2 \mathcal{E} - c^2 q^2)^2 \mathcal{E} = \left(\frac{2\alpha c b}{\pi}\right)^2 (\omega^2 \mathcal{E} - c^2 q_\perp^2), \qquad (9)$$

where $q = \sqrt{q_z^2 + q_\perp^2}$, and $q_\perp = \sqrt{q_x^2 + q_y^2}$ is the modulus of the radial component of the wave vector.

In the presence of an interface at $r = R$, the wave vector in the radial direction is not a conserved quantity, but is instead determined from (9) as a function of the axial momentum and the frequency. This yields real solutions, which correspond to the waveguide modes, as well as imaginary solutions $q_\perp = -i\kappa$, which decay exponentially from the interface toward the axis and are associated with the SPP modes. These are the object of this work and are characterized by the inverse localization length

$$\kappa_\pm = \sqrt{q_z^2 - \frac{\omega^2}{c^2}\mathcal{E} + \frac{2}{\mathcal{E}}\left(\frac{\alpha b}{\pi}\right)^2 \pm \frac{2\alpha b}{\pi}\sqrt{\frac{q_z^2}{\mathcal{E}} + \left(\frac{\alpha b}{\pi \mathcal{E}}\right)^2}}. \qquad (10)$$

The interface delimits a compact section of material, so that the light modes are labeled by the OAM [38], rather than the wave vector perpendicular to the light propagation. In Fig. 2 we show the dispersion relations for $\rho = 0.1$, $\beta = 10$. To understand these curves, let us start by noting that, when $cq_z/\omega_p \to \infty$, they all tend to the asymptotic value

$$\frac{\omega_\infty}{\omega_p} = \sqrt{\frac{\epsilon_W}{\epsilon_d + \epsilon_W}}, \qquad (11)$$

formally the same as for conventional metals [62]. However, in a WPW, a novel scaling regime appears, in which the longitudinal wave vector is coupled with the OAM,

$$\frac{\omega_m}{\omega_\infty} \simeq 1 + \frac{m\beta\sqrt{\frac{\epsilon_d + \epsilon_W}{\epsilon_W}} - \frac{\epsilon_d}{2}}{\epsilon_d + \epsilon_W} \frac{1}{Rq_z} + O\left(\frac{1}{R^2 q_z^2}\right), \qquad (12)$$
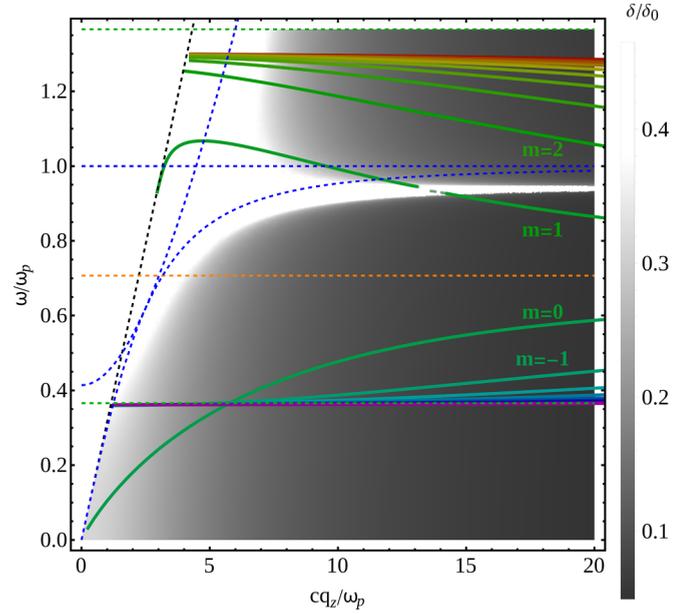

FIG. 2. Dispersion relations of the SPP modes of the cylindrical waveguide at small wave vector. For $\rho = 0.1$, $\beta = 10$, $\omega_c/\omega_p = 10$, $\omega_F/\omega_p = 1$, the shown modes have OAM label between $m = -10$ (lowest purple line) and $m = 10$ (highest red line), with color ordering. Background: SPP penetration length in units of the metal skin depth δ/δ_0 for $\epsilon_W = \epsilon_d = 10$. The dashing in the dispersions visible in the $m = 1$ line indicates a region where the modes do not have a surface component. The dashed guidelines represent analytical expressions, which we compare to the numerical solutions. We show the asymptotic lines (11) (orange) and (13) (green). We also show in blue the boundary of the region with mixed surface and bulk modes (14), as well as ω_p and the degeneracy line discussed below Eq. (14). The formulas are more accurate away from ω_p, but discrepancies always stay below 10%. All plasmonic dispersions end on the dispersion of the light in the dielectric medium (black dashed), on whose left they are not localized.

when $Rq_z \gg 1$, $m\beta\omega_p/\omega_\infty$. The asymmetry of the dispersion under $m \to -m$ in (12) quantifies the observed difference in curves and shows that there are modes with negative group velocity $v = d\omega/dq_z$. Equation (12), rigorously valid in the Drude approximation for the permittivity, is a good approximation for the full SPP dispersions as well, because typical SPP frequencies are around $\omega_\infty < \omega_p$; see Eq. (11). The limit $m \to \pm\infty$ at a fixed value of q_z identifies instead two distinct lines,

$$\frac{\omega_\pm}{\omega_p} = \frac{\epsilon_W}{\sqrt{\epsilon_W(\epsilon_W + \epsilon_d) + \beta^2} \mp \beta}, \qquad (13)$$

which are accumulation points for positive and negative OAM. While the dispersion with $m = 0$ is always the lowest-frequency mode in a metallic waveguide, this is not the case in a WPW. The SPP dispersions are symmetric under $q_z \to -q_z$. Our solution correctly reproduces the planar limit $R \to \infty$ and the normal metal limit $b \to 0$, known in implicit form [63,64].

IV. LIGHT PROPAGATION IN THE WPW

The SPP penetration in the WS bulk differs from that of its metallic counterpart [65]. Indeed, the inverse penetration lengths $\kappa_\pm$ in Eq. (10) have a finite imaginary part. More in detail, our solution is a superposition of two waves, each expressed in terms of modified Bessel functions. These behave approximately as an exponential, with a penetration depth given by $\delta_\pm = 1/\mathrm{Re}[\kappa_\pm]$. In Fig. 2, we compare the maximal penetration depth $\delta = \max_\pm \delta_\pm$ with the metal skin depth $\delta_0 = c/\omega_p$. The shorter wavelengths, on the right, are more localized. On the left, the localization length diverges on the line identified by the condition $\kappa_- = 0$; see Eq. (10). Using the Drude form of the permittivity (6), one obtains the analytic curve

$$\frac{\omega_{\mathrm{mix}}}{\omega_p} = \frac{1}{\epsilon_W}\left[\sqrt{\epsilon_W\left(\frac{c^2 q_z^2}{\omega_p^2} + \epsilon_W\right) + \beta^2} - \beta\right] \quad (14)$$

shown in the figure as a dashed blue line, also in good agreement with the numerical results obtained using the full permittivity. Between this line and the light dispersion, the modes have mixed character, a superposition between SPPs (exponentially localized) and waveguide (oscillating) modes. Purely waveguide modes are present in the roughly triangular region at the center of the figure, delimited by the plasma frequency and the degeneracy line identified by the condition $\kappa_+ = \kappa_-$. Outside of these regions, we have SPP modes. As can be seen in Fig. 2, our analytical expressions (11)–(14) are accurate approximations of the asymptotic behaviors as long as their value is away from ω_p. The exact value can be obtained by solving the pertinent asymptotic conditions numerically; see Appendix B. We also observe from Fig. 2 that the axionic term pushes down the frequency of the negative-m modes. Compared to a metal, this makes more SPP modes available at small wave vectors and frequencies.

The group velocity of the SPPs is computed as the derivative of the numerical dispersion. The axionic term generates a giant nonreciprocity in the group velocities, controlled by the OAM m, which is the main result of this work: modes with opposite values of m propagate with opposite group velocity in some regimes. The proposed device does not require a magnetic field to control the wave propagation [5]. We exemplify this observation in Fig. 3. Noticeably, the group velocities of the $m = \pm 2$ modes have opposite sign. Moreover, the $m = 1$ mode exhibits a zero and the associated sign change, shown in Fig. 3 around $cq_z/\omega_p \approx 5$, which signals the onset of the short-wavelength regime; see Eq. (12).

V. DISCUSSION

Our results show a strong effect due to the Weyl nodes on the SPP modes and a giant nonreciprocity under time-reversal, which inverts the OAM quantum number $m \rightarrow -m$. While the occurrence of the splitting of the bands with opposite m may be explained with the time-reversal symmetry breaking at a microscopic level by an intrinsic magnetization, in this class of materials the effect on the propagation velocity appears to be giant, as large as the velocity itself. To understand this, we underline that SPPs arise from the hybridization of electro-
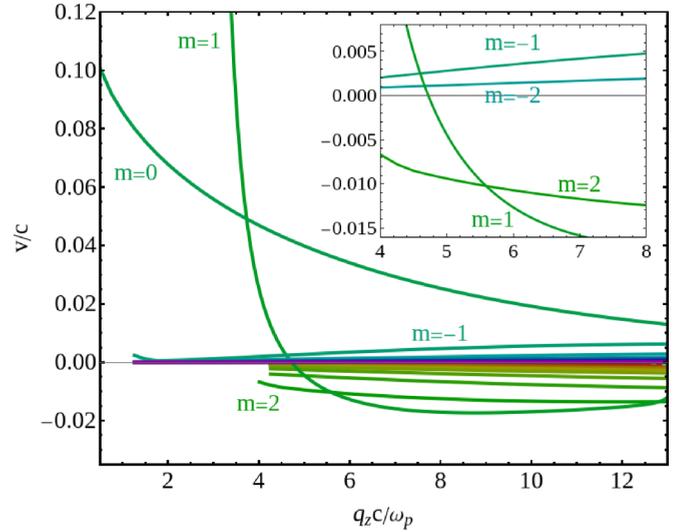

FIG. 3. SPP group velocity for $\rho = 0.1$, $\beta = 10$, $\omega_c/\omega_p = 10$, $\omega_F/\omega_p = 1$, for the modes between $m = -10$ (purple) and $m = 10$ (red), with color ordering (same color code as in Fig. 2). Inset: zero of the $m = 1$ mode and opposite velocities of the lowest OAM. The splitting due to the topological axion term is as large as the velocity itself and determines the change in sign.

magnetic and electronic modes. The semiclassical dynamics of the electrons in WSs is largely influenced by the Berry curvature [15,66]. As there is a net flux of Berry curvature in the region of the Brillouin zone between the Weyl nodes, one finds a nonzero expectation value of the electron angular momentum [67]. This is inherited by the radiation and determines a preferential sign of the OAM in the SPP dispersion [68]. The origin of the effect lies in the anomalous term proportional to **b** in (5) and in its macroscopic manifestation, the anomalous Hall effect. This term enters the off-diagonal permittivity and is responsible for the gyrotropic responses. To quantify the role of the node splitting, we can directly compare the anomalous Hall responses of a well-studied nontopological ferromagnet, Fe [69], with that of a well-studied topological Weyl semimetal, $Co_3Sn_2S_2$ [70]. Using the values provided in these references for the AHE, we expect an enhancement of at least 50% in the latter material. We also point out that various electronic scattering mechanisms may destroy these surface plasmon features in ordinary ferromagnets. Conversely, the effect may be observable in Weyl semimetals, in which the band topology, the surface states, and the associated anomalous Hall effect are robust against weak scattering, e.g., with phonons [71,72]. The effect studied in this work differs qualitatively from previously noted asymmetries in SPP dispersions, as it does not require changing the orientation of the incoming beam, nor the configuration of the guide [30,73–76]. Conversely, a compact transverse size is essential. In infinite slab geometries, depending on the propagation direction, one would instead observe either reciprocal dispersion or opposite nonreciprocities on the opposite interface, leading to a cancellation of the net effect of the nodes. The SPP nonreciprocity qualitatively differs from the Faraday (Kerr) rotation [23] in that it relates the beam OAM and its propagation, as opposed to its polarization. Our analysis exploits the long-wavelength

approximation of the dielectric function, which is valid for $\omega \ll \omega_F$ [28]. While we do not expect qualitative changes in the discussed regimes, inclusion of the q-dependence in the permittivity would allow us to obtain quantitatively more accurate dispersion curves and to explore larger wave vectors [27,28].

Our result does not rely on a specific material in which the Weyl semimetal phase is realized. A way of testing our predictions is to excite the different SPP modes via Laguerre-Gaussian beams, which carry definite OAM [77–79] or illuminated metal tips [16]. Detection may exploit the strong coupling of the SPP modes to quantum dots [80] or that the waveguide can filter out one sign of the OAM. Alternative platforms for realizing the SPP nonreciprocity, as well as the light-induced phenomena in OAM-filtered light, are a few of the many interesting open questions. The proposed plasmon waveguide can be scaled down to nanometer size and operate down to THz frequencies while retaining the described efficient control mechanism. Such a device is central to many applications, including nanocircuits, holography, nanosensors, and nanophotonics [3,81–85], and it may find use in classical communication between quantum architectures and on-chip isolation [86]. The ability to control SSP propagation at the nanoscale holds significant promise for advancing both classical and quantum technologies.

DATA AVAILABILITY

The data that support the findings of this article are openly available [87].

APPENDIX A: SOLUTION OF AXION ELECTRODYNAMICS

In this appendix, we provide some detail about the solution of the set of axion electrodynamics equations (2)–(5) in cylindrical coordinates. It is useful to manipulate the latter and bring it to the form

$$\nabla \times \mathbf{B} = -i\frac{\omega}{c^2}\mathcal{E}\mathbf{E} - \frac{2\alpha}{\pi c}\mathbf{b} \times \mathbf{E}. \tag{A1}$$

Taking the curl of Eq. (3) and using Eq. (5), one obtains the wave equation

$$\mathbf{0} = \nabla(\nabla \cdot \mathbf{E}) - \Delta\mathbf{E} - Q^2\mathbf{E} + i\omega\frac{2\alpha}{\pi c}\mathbf{b} \times \mathbf{E}, \tag{A2}$$

where $Q^2 = \frac{\omega^2 \mathcal{E}(\omega)}{c^2}$. Choosing the z axis along the main axis of the material, the wave-vector component q_z parallel to the Weyl node separation vector $2\mathbf{b}$ is conserved. Moreover, the cylindrical symmetry implies that the electric field can be chosen as an eigenstate of the generator of rotations around the z axis,

$$J_z = -i\partial_\varphi + \Sigma_z, \qquad \Sigma_z = \begin{pmatrix} 0 & -i & 0 \\ i & 0 & 0 \\ 0 & 0 & 1 \end{pmatrix}. \tag{A3}$$

It follows that it must have the dependence $\sim e^{im\varphi}$ on the angular variable φ, and its components must take the form

$$\begin{aligned} E_r(r) &= f(r) + g(r), \\ E_\varphi(r) &= if(r) - ig(r), \\ E_z(r) &= h(r), \end{aligned} \tag{A4}$$

where $f(r), g(r), h(r)$ are complex functions of the radial coordinate r. Guided by the solution in the metallic limit $\mathbf{b} = 0$, one can make the ansatz

$$\begin{aligned} E_r &= A_m\mathcal{D}_{m-1}(q_\perp r) + B_m\mathcal{D}_{m+1}(q_\perp r), \\ E_\varphi &= iA_m\mathcal{D}_{m-1}(q_\perp r) - iB_m\mathcal{D}_{m+1}(q_\perp r), \\ E_z &= C_m\mathcal{D}_m(q_\perp r), \end{aligned} \tag{A5}$$

where $\mathcal{D}_m$ denotes any Bessel function of the first kind of order m, and $q_\perp$ is a parameter, generally complex, that is to be determined. In the bulk problem, $q_\perp$ is the modulus of the radial component of the momentum, $q_\perp = \sqrt{q_x^2 + q_y^2}$. With the above ansatz, the modified Maxwell equations yield algebraic equations in the unknown coefficients A_m, B_m, C_m. In particular, Eq. (2) becomes

$$-q_\perp(1 - b_\omega)A_m + q_\perp(1 + b_\omega)B_m + iq_zC_m = 0, \tag{A6}$$

having defined the frequency-dependent dimensionless constant $b_\omega = 2\alpha bc/\pi\omega\mathcal{E}$. We then write (A2) as the linear system

$$\begin{pmatrix} Q^2 - q^2 - b_\omega\left(Q^2 - \frac{q_\perp^2}{2}\right) & \frac{q_\perp^2}{2}b_\omega & 0 \\ -\frac{q_\perp^2}{2}b_\omega & Q^2 - q^2 + b_\omega\left(Q^2 - \frac{q_\perp^2}{2}\right) & 0 \\ ib_\omega q_\perp q_z & ib_\omega q_\perp q_z & Q^2 - q^2 \end{pmatrix} \begin{pmatrix} A_m \\ B_m \\ C_m \end{pmatrix} = \begin{pmatrix} 0 \\ 0 \\ 0 \end{pmatrix}. \tag{A7}$$

To find a nontrivial solution to (A7), the determinant of the matrix above must vanish. This directly leads to the condition (9) in the main text, which implicitly determines the dispersion relation of bulk modes [29]. One finds two linearly independent electric field eigenmodes whose components are determined from the solution of (A6) and (A7). They can be written in the form

$$\mathbf{E}_m = a_m \begin{pmatrix} \frac{m}{q_\perp r}\mathcal{D}_m \\ i\mathcal{D}'_m \\ 0 \end{pmatrix} + b_m \begin{pmatrix} \mathcal{D}'_m \\ \frac{im}{q_\perp r}\mathcal{D}_m \\ -\frac{iq_z q_\perp}{Q^2 - q_\perp^2}\mathcal{D}_m \end{pmatrix} \quad \text{(A8)}$$

in which the coefficients $a_m = A_m + B_m$, $b_m = A_m - B_m$ are constrained by (A6) and (A7).

Analytic continuation $q_\perp \to -i\kappa$ allows us to describe modes that are exponentially localized at the WS-dielectric interface. For this class of solutions, the electric field is written as $\mathbf{E}_m = \sum_{s=\pm} a_s^{(m)} \mathbf{E}_{m,s}$, where the modes labeled by $s = \pm$ are

$$\mathbf{E}_{m,s} = \frac{\omega}{q_z}\left[\begin{pmatrix} \frac{im}{\kappa_s r}I_m(\kappa_s r) \\ -I'_m(\kappa_s r) \\ 0 \end{pmatrix} + \gamma_s \begin{pmatrix} iI'_m(\kappa_s r) \\ -\frac{m}{\kappa_s r}I_m(\kappa_s r) \\ \frac{c\,q_z\kappa_s}{Q^2+\kappa_s^2}I_m(\kappa_s r) \end{pmatrix} \right], \quad \text{(A9)}$$

in which the Bessel functions of the second kind I_m are regular in the origin and

$$\gamma_\pm = \frac{1}{\overline{Q}}\left(\frac{\beta}{\sqrt{\mathcal{E}}} \pm \sqrt{\overline{q}_z^2 + \left(\frac{\beta}{\sqrt{\mathcal{E}}}\right)^2} \right). \quad \text{(A10)}$$

Here and in the following, we denote the wave vectors in units of ω_p/c as $\overline{q}_z = q_z c/\omega_p$ and $\overline{Q} = Qc/\omega_p$. In the two solutions, the index s appears in the argument of the Bessel functions and determines the localization length as discussed in the main text. The magnetic field is readily computed via Eq. (3) in the frequency domain as

$$\mathbf{B}_{m,s} = \begin{pmatrix} I'_m(\kappa_s r) \\ \frac{im}{\kappa_s r}I_m(\kappa_s r) \\ \frac{i\kappa_s}{q_z}I_m(\kappa_s r) \end{pmatrix} + \frac{1}{\gamma_s} \begin{pmatrix} \frac{im}{\kappa_s r}I_m(\kappa_s r) \\ iI'_m(\kappa_s r) \\ 0 \end{pmatrix}. \quad \text{(A11)}$$

Because of the chosen parametrization, our solution contains a curve, identified by the condition $\kappa_+ = \kappa_-$, in which the two modes with $s = \pm$ are not linearly independent. The degeneracy curve is defined from Eq. (10) by the condition

$$\overline{q}_z^2 \mathcal{E} + \beta^2 = 0. \quad \text{(A12)}$$

Using the single-band approximation, i.e., retaining only the first term in the permittivity (6), one finds

$$\omega_{\text{deg}}(q_z) \approx \frac{\sqrt{\epsilon_W}\,\omega_p}{\sqrt{\epsilon_W + \beta^2/\overline{q}_z^2}}. \quad \text{(A13)}$$

This is a good approximation as long as $\omega_{\text{deg}} \ll \omega_p$.

The field in the outer region is well known [63,64]. Again, we focus on evanescent solutions in the radial direction

and write it as the superposition $\mathbf{E}_m^{(\text{out})} = b_1^{(m)}\mathbf{E}_{m,1} + b_2^{(m)}\mathbf{E}_{m,2}$, where

$$\mathbf{E}_{m,1} = \frac{i\omega}{q_z}\begin{pmatrix} \frac{m}{\kappa_d r}K_m(\kappa_d r) \\ iK'_m(\kappa_d r) \\ 0 \end{pmatrix}, \quad \text{(A14)}$$

$$\mathbf{E}_{m,2} = \begin{pmatrix} K'_m(\kappa_d r) \\ \frac{im}{\kappa_d r}K_m(\kappa_d r) \\ \frac{i\kappa_d}{q_z}K_m(\kappa_d r) \end{pmatrix}. \quad \text{(A15)}$$

Here the functions K_m are regular as $r \to \infty$ and, in fact, exponentially decaying, with inverse decay length $\kappa_d = \sqrt{q_z^2 - Q_d^2}$ and $Q_d = \omega\sqrt{\epsilon_d}/c$. The corresponding magnetic field is computed by means of the usual Maxwell-Faraday equation as

$$\mathbf{B}_{m,1} = \begin{pmatrix} K'_m(\kappa_d r) \\ \frac{im}{\kappa_d r}K_m(\kappa_d r) \\ \frac{i\kappa_d}{q_z}K_m(\kappa_d r) \end{pmatrix}, \quad \text{(A16)}$$

$$\mathbf{B}_{m,2} = \frac{Q_d^2}{q_z^2}\begin{pmatrix} \frac{m}{\kappa_d r}K_m(\kappa_d r) \\ iK'_m(\kappa_d r) \\ 0 \end{pmatrix}. \quad \text{(A17)}$$

APPENDIX B: BOUNDARY CONDITIONS FOR THE METAL-DIELECTRIC INTERFACE

1. Derivation of the boundary conditions

We now provide some details about the manipulations of the modified electrodynamics equations. The modified Ampère-Maxwell law follows:

$$\nabla \times \mathbf{B} = -i\frac{\omega}{c^2}\mathbf{E} + \mu_0\mathbf{j}_e - \frac{2\alpha}{\pi c}\mathbf{b} \times \mathbf{E}. \quad \text{(B1)}$$

It is customary to divide the current in the source term into the contributions from free and bound charges

$$\mathbf{j}_e = \mathbf{j}_f + \mathbf{j}_p = \sigma\mathbf{E} - i\omega\mathbf{P}. \quad \text{(B2)}$$

As we are considering a magnetic WS, no magnetization current is present in this expression. In general, it can be present in the dielectric and handled in a standard way. For a linear material, the polarization is proportional to the applied field $\mathbf{P} = \varepsilon_0\chi_e\mathbf{E}$, and (B1) becomes

$$\nabla \times \mathbf{B} = -i\frac{\omega}{c^2}\mathcal{E}\mathbf{E} - \frac{2\alpha}{\pi c}\mathbf{b} \times \mathbf{E} \quad \text{(B3)}$$

with $\varepsilon_0\mathcal{E} = \varepsilon_0\epsilon_W + i\sigma/\omega$.

Let us consider an interface at $r = R$. Following the viewpoint of [88], we derive the boundary condition on the macroscopic fields to lowest order in a gradient expansion. The localized contributions to charge and current density have been considered in [24] and found to be not relevant for this class of problems in the small wave-vector regime. Integrating Eq. (B3) across the interface, one establishes the continuity of the components of the magnetic field. This does not exclude a static uniform magnetization of the material; see [89]. We note that the contribution of the magnetization current is neglected throughout the paper, $\nabla \times \mathbf{M} \approx \mathbf{0}$. In symbols,

$$\mathbf{B}_\parallel(r = R^+) = \mathbf{B}_\parallel(r = R^-). \quad \text{(B4)}$$

We approximate the corresponding magnetic constant as $\mu_d \approx \mu_0$. The above equation is therefore equivalent to the continuity of the magnetic field parallel to the interface, while straightforward modifications are necessary in the most general case. Using $\nabla \cdot \mathbf{P} = -\rho_b$, with ρ_b the density of bound charge, one writes the total charge density as the sum of free and bound contributions,

$$\rho_e = \rho_b + \rho_f = -\nabla \cdot \left(\varepsilon_0 \chi_e \mathbf{E} + \frac{i\sigma}{\omega} \mathbf{E} \right). \tag{B5}$$

Defining the electric displacement in the WS as

$$\mathbf{D} = \left(\varepsilon_0 \mathcal{E} \mathbf{E} + \frac{2\alpha c \varepsilon_0}{\pi i \omega} \mathbf{b} \times \mathbf{E} \right) \tag{B6}$$

and in the dielectric as $\mathbf{D} = \epsilon_d \varepsilon_0 \mathbf{E}$, Eq. (2) can be cast in the form

$$\nabla \cdot \mathbf{D} = 0. \tag{B7}$$

Integrating the previous equation across the interface, one obtains the continuity of the component perpendicular to the interface,

$$\mathbf{D}_\perp(r = R^+) = \mathbf{D}_\perp(r = R^-). \tag{B8}$$

Integration of the homogeneous Maxwell equations (3) and (4) across the interface determines the continuity of the components of the electric field parallel to the interface,

$$\mathbf{E}_\parallel(r = R^+) = \mathbf{E}_\parallel(r = R^-) \tag{B9}$$

and of the magnetic field perpendicular to it,

$$\mathbf{B}_\perp(r = R^+) = \mathbf{B}_\perp(r = R^-). \tag{B10}$$

2. Imposing the boundary conditions

Let us now consider the WS-dielectric interface at $r = R$. We have established that the electric field inside the semimetallic cylinder is a linear superposition of the modes (A9), with coefficients $a_\pm^{(m)}$, while in the dielectric outside it is a linear superposition of the modes (A14), with coefficients $b_{1,2}$.

As the Maxwell equations completely determine the magnetic field once the electric field is known, three conditions are needed at the dielectric-WS interface. A more compact form is obtained by instead imposing four conditions and requiring that they are compatible among them [64]. The continuity of the tangential components of the electric field and of the magnetic induction, in particular, results in a linear system for the four unknown coefficients $\mathbf{c}_m = (a_+^{(m)}, a_-^{(m)}, b_1^{(m)}, b_2^{(m)})$. After an appropriate rescaling of the coefficients, the system can be cast in the form $B_m \mathbf{c}_m = 0$, with the matrix

$$B_m = \begin{pmatrix} \frac{I'_m(u_+)}{I_m(u_+)} + \frac{\gamma_+ m}{u_+} & \frac{I'_m(u_-)}{I_m(u_-)} + \frac{\gamma_- m}{u_-} & \frac{K'_m(v)}{K_m(v)} & \frac{m}{v} \\ \frac{u_+}{\gamma_+} \frac{q_z^2}{Q^2} & \frac{u_-}{\gamma_-} \frac{q_z^2}{Q^2} & 0 & v \\ \frac{I'_m(u_+)}{\gamma_+ I_m(u_+)} + \frac{m}{u_+} & \frac{I'_m(u_-)}{\gamma_- I_m(u_-)} + \frac{m}{u_-} & \frac{m}{v} & \frac{Q_d^2}{q_z^2} \frac{K'_m(v)}{K_m(v)} \\ u_+ & u_- & v & 0 \end{pmatrix}. \tag{B11}$$

The arguments of the Bessel functions are denoted as

$$u_\pm = \kappa_\pm R = \rho \sqrt{\overline{q}_z^2 - \overline{Q}^2 + \frac{2\beta^2}{\mathcal{E}} \pm \frac{2\beta}{\sqrt{\mathcal{E}}} \sqrt{\overline{q}_z^2 + \frac{\beta^2}{\mathcal{E}}}} \tag{B12}$$

and

$$v = \kappa_d R = \rho \sqrt{\overline{q}_z^2 - \overline{Q}_d^2}. \tag{B13}$$

The boundary conditions can only be consistently satisfied if the determinant of this matrix vanishes, which amounts to the condition

$$\det B_m(\omega, q_z) = 0. \tag{B14}$$

This equation implicitly determines the dispersion curves $\omega = \omega_m(q_z)$. As for the metallic waveguide, it must be solved numerically in the general case. In the next section, we provide useful starting points for the root-finding routines. The solutions with $-10 \leqslant m \leqslant 10$ are illustrated for sample parameters in Fig. 4.

We note that the SPPs obtained by solving Eq. (B14) propagate along the direction of the separation between the Weyl nodes. This situation corresponds to a Faraday configuration, where, in a planar slab, the modes are reciprocal [30]. In our case, the dispersions remain symmetric under inversion

of q_z but become nonreciprocal with respect to the angular momentum m.

APPENDIX C: ASYMPTOTIC REGIMES

a. Metallic limit

We check now that the limit $b \to 0$ (or, equivalently, $\beta \to 0$) correctly reproduces the plasmonic dispersion of the metallic waveguide. In such a limit, the arguments of the Bessel functions in (B12) tend to the same expression $u_\pm \to u = R\sqrt{q_z^2 - Q^2}$, which is the corresponding value in a metal [64]. In the same limit $\gamma_\pm \to \pm\gamma$, where $\gamma = \sqrt{q_z^2/Q^2}$. The determinant of (B11) is most easily computed by replacing the first two columns by linear combinations, namely semisum and semidifference, so that one arrives at the matrix

$$B_m^{(0)} = \begin{pmatrix} \frac{I'_m(u)}{I_m(u)} & \frac{\gamma m}{u} & \frac{K'_m(v)}{K_m(v)} & \frac{m}{v} \\ 0 & \frac{u}{\gamma} \frac{q_z^2}{Q^2} & 0 & v \\ \frac{m}{u} & \frac{I'_m(u)}{\gamma I_m(u)} & \frac{m}{v} & \frac{Q_d^2}{q_z^2} \frac{K'_m(v)}{K_m(v)} \\ u & 0 & v & 0 \end{pmatrix}. \tag{C1}$$
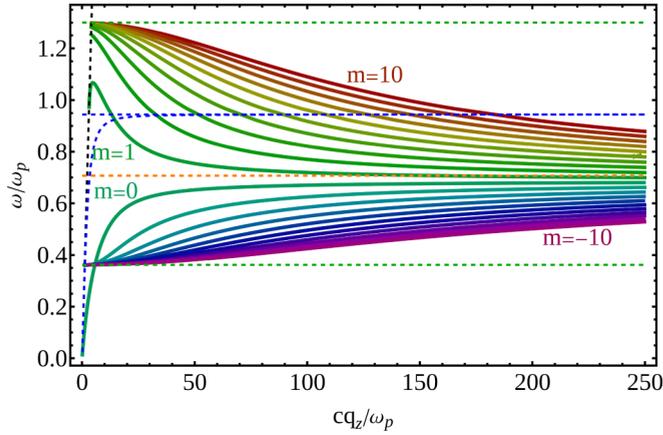
FIG. 4. Crossover in the SPP dispersions for $\beta = 10$, $\rho = 0.1$, $\omega_c/\omega_p = 10$, $\omega_F/\omega_p = 1$. The vertical order of the negative-m solutions as $q_z \to \infty$ is inverted with respect to the order at $q_z \to 0$. The green dashed lines are the $m \to \pm\infty$ asymptotes from (C16), the blue dashed lines are the plasma frequency computed from the full permittivity (6) and the degeneracy line $\kappa_+ = \kappa_-$, while the orange dashed line is the large-wave-vector limit computed from (C13).

The condition $\det B_m^{(0)} = 0$ is exactly the one that implicitly defines the frequencies of the SPP modes in a metal [63].

b. Planar limit

To make contact with known results [29,30,61], we now discuss the planar limit of the cylindrical waveguide. We set the wave vector in the angular direction $q_y = m/R$ and take the limit $R \to \infty$ and $|m| \to \infty$, while keeping their ratio q_y fixed. Then the factor $e^{im\varphi}$ directly maps into the plane wave $e^{iq_y y}$, with $y = R\varphi$. The radial and azimuthal versors $\hat{r}$ and $\hat{\varphi}$ are mapped into the versors $\hat{x}$ and $\hat{y}$, respectively. Next, we need to calculate the limit of the ratios

$$\frac{I'_m(\kappa_\pm R)}{I_m(\kappa_\pm R)}, \quad \frac{K'_m(\kappa_d R)}{K_m(\kappa_d R)}. \tag{C2}$$

We focus on the first ratio above; for the second, the calculation is essentially the same and we only give the final result. Omitting for notational simplicity the index $\pm$, we set $v = |m| = R|q_y|$, $t = \kappa/|q_y|$ and write

$$\frac{I'_{|m|}(\kappa R)}{I_{|m|}(\kappa R)} = \frac{I'_v(vt)}{I_v(vt)} = \frac{1}{v}\frac{d}{dt}\ln I_v(vt). \tag{C3}$$

We also define

$$\mu_\pm = \sqrt{q_y^2 + \kappa_\pm^2}, \quad \mu_d = \sqrt{q_y^2 + \kappa_d^2},$$

which are inverse decay lengths in the x-direction, corresponding to the evanescent waves $e^{\mu_\pm x}$ and $e^{-\mu_d x}$ of the planar geometry. We recall the homogeneous expansions of the modified Bessel functions [90],

$$I_v(vt) \sim \frac{e^{v\eta_t}}{(2\pi v)^{1/2}(1+t^2)^{1/4}}, \tag{C4}$$

$$K_v(vt) \sim \frac{\pi e^{-v\eta_t}}{(2\pi v)^{1/2}(1+t^2)^{1/4}}, \tag{C5}$$

where

$$\eta_t = \sqrt{1+t^2} + \ln\frac{t}{1+\sqrt{1+t^2}}, \tag{C6}$$

$$p_t = \frac{1}{\sqrt{1+t^2}}. \tag{C7}$$

These expansions hold uniformly for $0 < t < \infty$ as $v \to +\infty$. Using (C4), we obtain

$$\frac{I'_m(\kappa R)}{I_m(\kappa R)} \sim \frac{d\eta_t}{dt} = \frac{\sqrt{q_y^2 + \kappa^2}}{\kappa}, \tag{C8}$$

$$\frac{K'_m(\kappa_d R)}{K_m(\kappa_d R)} \sim -\frac{d\eta_t}{dt} = -\frac{\sqrt{q_y^2 + \kappa_d^2}}{\kappa_d}. \tag{C9}$$

Restoring the label $s = \pm$, the matrix encoding the interface conditions becomes

$$B_m \to \begin{pmatrix} \mu_+ + \gamma_+ q_y & \mu_- + \gamma_- q_y & -\mu_d & q_y \\ \frac{(-\mu_+^2 + q_y^2)q_z^2}{\gamma_+ Q^2} & \frac{(-\mu_-^2 + q_y^2)q_z^2}{\gamma_- Q^2} & 0 & -\mu_d^2 + q_y^2 \\ q_y + \frac{\mu_+}{\gamma_+} & q_y + \frac{\mu_-}{\gamma_-} & q_y & -\frac{Q_d^2}{q_z^2}\mu_d \\ -\mu_+^2 + q_y^2 & -\mu_-^2 + q_y^2 & -\mu_d^2 + q_y^2 & 0 \end{pmatrix}, \tag{C10}$$

This matrix coincides with the one obtained for the half-space geometry, with the WS with $\mathbf{b} = b\hat{z}$ in the region $x < 0$ and the dielectric in the region $x > 0$ [29].

c. Limit of large wave vector

We provide here some detail about the large-wave-vector limit (12). We make use of the asymptotic expansions of the Bessel functions of the second kind for large argument z [90],

$$\frac{I'_m(z)}{I_m(z)} \sim 1 - \frac{1}{2z}, \tag{C11}$$

$$\frac{K'_m(z)}{K_m(z)} \sim -1 - \frac{1}{2z}. \tag{C12}$$

Expanding (B12) and (B13), one arrives at the expression

$$\det M_m \sim -4q_z R(Q^2 + Q_d^2) + 2(Q^2 - Q_d^2) + 8Q\frac{m\alpha b}{\pi\sqrt{\mathcal{E}}}. \tag{C13}$$

Substituting the definitions of Q and Q_d and solving the vanishing condition of the determinant in ω with the high-frequency, single-band approximation for the dielectric function, one finds Eq. (12). The asmptotic limit as computed from Eq. (C13) is shown as an orange dashed line in Fig. 4.

d. Limit of large angular momentum

We consider now the limit $m \to \pm\infty$ at fixed wave vector. We need the identities

$$\frac{I'_m(u)}{I_m(u)} \sim \frac{|m|}{u}, \quad \frac{K'_m(v)}{K_m(v)} \sim -\frac{|m|}{v} \tag{C14}$$

for the order of the Bessel functions $m \to \pm\infty$. After some algebra, one obtains Eq. (B14) in the form

$$[\overline{\omega}(\epsilon_d + \mathcal{E}) - 2\,\text{sgn}(m)\beta][\overline{q}_z^2 - \overline{\omega}^2\mathcal{E} - 2\,\text{sgn}(m)\beta\overline{\omega}] = 0, \tag{C15}$$

apart from an overall factor, different from zero. (We use the notation $\overline{\omega} = \omega/\omega_p$.) Requiring that the solutions have a nondiverging localization length and reproduce the results for the metallic cylinder in the limit $\beta \to 0$ implies that the $m \to \pm\infty$ asymptotes must satisfy

$$\overline{\omega}(\epsilon_d + \mathcal{E}) - 2\,\text{sgn}(m)\beta = 0. \qquad (C16)$$

In general, this has to be solved numerically, but a good approximation is obtained when retaining only the first term in Eq. (6), which yields the $\omega_\pm$ in Eq. (13) of the main text. The

numerical solutions of Eq. (C16) are instead shown in Fig. 4 as green dashed lines.

APPENDIX D: PARAMETERS

As an example, we consider the set of parameters $E_F \approx 0.04\,\text{eV}$, $v_F = 10^5\,\text{m/s}$, $\omega_F \approx 6.1 \times 10^{13}\,\text{Hz}$, $E_c \approx 0.2\,\text{eV}$, $\omega_p \approx 5.8 \times 10^{13}\,\text{Hz}$, modeled on $EuCd_2As_2$ [42–44]; see also [13,14,91]. One finds $\omega_c/\omega_p \sim 5$, $\omega_F/\omega_p \sim 1$ and $\beta \sim 7$. The parameter $\rho = 0.1$ used in the main text corresponds to a cylinder of $R \approx 0.5\,\mu\text{m}$. The high-frequency skin depth is then estimated as $\delta_0 \sim 5\,\mu\text{m}$ and reference wave vector $\omega_p/c \sim 2 \times 10^5\,\text{m}^{-1}$. The minimal wavelength in Fig. 3 is therefore in the visible range.

[1] H. Yu, Y. Peng, Y. Yang, and Z.-Y. Li, Plasmon-enhanced light–matter interactions and applications, npj Comput. Mater. **5**, 45 (2019).

[2] R. F. Oulton, V. J. Sorger, T. Zentgraf, R.-M. Ma, C. Gladden, L. Dai, G. Bartal, and X. Zhang, Plasmon lasers at deep subwavelength scale, Nature (London) **461**, 629 (2009).

[3] D. K. Gramotnev and S. I. Bozhevolnyi, Plasmonics beyond the diffraction limit, Nat. Photon. **4**, 83 (2010).

[4] M. T. Hill, M. Marell, E. S. P. Leong, B. Smalbrugge, Y. Zhu, M. Sun, P. J. van Veldhoven, E. J. Geluk, F. Karouta, Y.-S. Oei, R. Nötzel, C.-Z. Ning, and M. K. Smit, Lasing in metal-insulator-metal sub-wavelength plasmonic waveguides, Opt. Express **17**, 11107 (2009).

[5] R. Camley, Nonreciprocal surface waves, Surf. Sci. Rep. **7**, 103 (1987).

[6] J. Lin, J. P. B. Mueller, Q. Wang, G. Yuan, N. Antoniou, X.-C. Yuan, and F. Capasso, Polarization-controlled tunable directional coupling of surface plasmon polaritons, Science **340**, 331 (2013).

[7] Y. Liu, S. Palomba, Y. Park, T. Zentgraf, X. Yin, and X. Zhang, Compact magnetic antennas for directional excitation of surface plasmons, Nano Lett. **12**, 4853 (2012).

[8] L. Huang, X. Chen, B. Bai, Q. Tan, G. Jin, T. Zentgraf, and S. Zhang, Helicity dependent directional surface plasmon polariton excitation using a metasurface with interfacial phase discontinuity, Light Sci. Appl. **2**, e70 (2013).

[9] N. P. Armitage, E. J. Mele, and A. Vishwanath, Weyl and Dirac semimetals in three-dimensional solids, Rev. Mod. Phys. **90**, 015001 (2018).

[10] S.-Y. Xu, I. Belopolski, N. Alidoust, M. Neupane, G. Bian, C. Zhang, R. Sankar, G. Chang, Z. Yuan, C.-C. Lee *et al.*, Discovery of a Weyl fermion semimetal and topological Fermi arcs, Science **349**, 613 (2015).

[11] B. Q. Lv, H. M. Weng, B. B. Fu, X. P. Wang, H. Miao, J. Ma, P. Richard, X. C. Huang, L. X. Zhao, G. F. Chen, Z. Fang, X. Dai, T. Qian, and H. Ding, Experimental discovery of Weyl semimetal taas, Phys. Rev. X **5**, 031013 (2015).

[12] J. Kruthoff, J. de Boer, J. van Wezel, C. L. Kane, and R.-J. Slager, Topological classification of crystalline insulators through band structure combinatorics, Phys. Rev. X **7**, 041069 (2017).

[13] B. Bradlyn, L. Elcoro, J. Cano, M. G. Vergniory, Z. Wang, C. Felser, M. I. Aroyo, and B. A. Bernevig, Topological quantum chemistry, Nature (London) **547**, 298 (2017).

[14] M. Vergniory, L. Elcoro, C. Felser, N. Regnault, B. A. Bernevig, and Z. Wang, A complete catalogue of high-quality topological materials, Nature (London) **566**, 480 (2019).

[15] D. T. Son and B. Z. Spivak, Chiral anomaly and classical negative magnetoresistance of Weyl metals, Phys. Rev. B **88**, 104412 (2013).

[16] F. M. D. Pellegrino, M. I. Katsnelson, and M. Polini, Helicons in Weyl semimetals, Phys. Rev. B **92**, 201407(R) (2015).

[17] F. Wilczek, Two applications of axion electrodynamics, Phys. Rev. Lett. **58**, 1799 (1987).

[18] A. Sekine and K. Nomura, Axion electrodynamics in topological materials, J. Appl. Phys. **129**, 141101 (2021).

[19] K. Fujikawa and H. Suzuki, *Path Integrals and Quantum Anomalies*, International Series of Monographs on Physics (Oxford University Press, Oxford, 2004).

[20] A. A. Zyuzin and A. A. Burkov, Topological response in Weyl semimetals and the chiral anomaly, Phys. Rev. B **86**, 115133 (2012).

[21] M. M. Vazifeh and M. Franz, Electromagnetic response of Weyl semimetals, Phys. Rev. Lett. **111**, 027201 (2013).

[22] Y. Chen, S. Wu, and A. A. Burkov, Axion response in Weyl semimetals, Phys. Rev. B **88**, 125105 (2013).

[23] M. Kargarian, M. Randeria, and N. Trivedi, Theory of Kerr and Faraday rotations and linear dichroism in topological Weyl semimetals, Sci. Rep. **5**, 12683 (2015).

[24] Q. Chen, A. R. Kutayiah, I. Oladyshkin, M. Tokman, and A. Belyanin, Optical properties and electromagnetic modes of Weyl semimetals, Phys. Rev. B **99**, 075137 (2019).

[25] V. S. Asadchy, C. Guo, B. Zhao, and S. Fan, Subwavelength passive optical isolators using photonic structures based on Weyl semimetals, Adv. Opt. Mater. **8**, 2000100 (2020).

[26] J. C. W. Song and M. S. Rudner, Fermi arc plasmons in Weyl semimetals, Phys. Rev. B **96**, 205443 (2017).

[27] G. M. Andolina, F. M. D. Pellegrino, F. H. L. Koppens, and M. Polini, Quantum nonlocal theory of topological Fermi arc plasmons in Weyl semimetals, Phys. Rev. B **97**, 125431 (2018).

[28] J. Zhou, H.-R. Chang, and D. Xiao, Plasmon mode as a detection of the chiral anomaly in Weyl semimetals, Phys. Rev. B **91**, 035114 (2015).

[29] J. Hofmann and S. Das Sarma, Surface plasmon polaritons in topological Weyl semimetals, Phys. Rev. B **93**, 241402(R) (2016).

[30] O. V. Kotov and Y. E. Lozovik, Giant tunable nonreciprocity of light in Weyl semimetals, Phys. Rev. B **98**, 195446 (2018).

[31] T. Tamaya, T. Kato, K. Tsuchikawa, S. Konabe, and S. Kawabata, Surface plasmon polaritons in thin-film Weyl semimetals, J. Phys.: Condens. Matter **31**, 305001 (2019).

[32] S. Oskoui Abdol, A. S. Vala, and B. Abdollahipour, Tunable surface plasmon polaritons in a Weyl semimetal waveguide, J. Phys.: Condens. Matter **31**, 335002 (2019).

[33] S. Oskoui Abdol, S. Shojaei, and B. Abdollahipour, Polarization dependent light propagation in WTe$_2$ multilayer structure, Sci. Rep. **13**, 13169 (2023).

[34] A. A. Zyuzin and V. A. Zyuzin, Chiral electromagnetic waves in Weyl semimetals, Phys. Rev. B **92**, 115310 (2015).

[35] X. Lu, D. K. Mukherjee, and M. O. Goerbig, Surface plasmonics of Weyl semimetals, Phys. Rev. B **104**, 155103 (2021).

[36] C. Guo, V. S. Asadchy, B. Zhao, and S. Fan, Light control with Weyl semimetals, eLight **3**, 2 (2023).

[37] P. O. Sukhachov and L. I. Glazman, Anomalous electromagnetic field penetration in a Weyl or Dirac semimetal, Phys. Rev. Lett. **128**, 146801 (2022).

[38] L. Allen, M. W. Beijersbergen, R. J. C. Spreeuw, and J. P. Woerdman, Orbital angular momentum of light and the transformation of laguerre-gaussian laser modes, Phys. Rev. A **45**, 8185 (1992).

[39] N. Matsumoto, T. Ando, T. Inoue, Y. Ohtake, N. Fukuchi, and T. Hara, Generation of high-quality higher-order laguerre-gaussian beams using liquid-crystal-on-silicon spatial light modulators, J. Opt. Soc. Am. A **25**, 1642 (2008).

[40] A. V. Akimov, A. Mukherjee, C. L. Yu, D. E. Chang, A. S. Zibrov, P. R. Hemmer, H. Park, and M. D. Lukin, Generation of single optical plasmons in metallic nanowires coupled to quantum dots, Nature (London) **450**, 402 (2007).

[41] A. V. Krasavin and A. V. Zayats, Silicon-based plasmonic waveguides, Opt. Express **18**, 11791 (2010).

[42] L.-L. Wang, N. H. Jo, B. Kuthanazhi, Y. Wu, R. J. McQueeney, A. Kaminski, and P. C. Canfield, Single pair of Weyl fermions in the half-metallic semimetal EuCd$_2$As$_2$, Phys. Rev. B **99**, 245147 (2019).

[43] J. Krishna, T. Nautiyal, and T. Maitra, First-principles study of electronic structure, transport, and optical properties of eucd$_2$as$_2$, Phys. Rev. B **98**, 125110 (2018).

[44] H. P. Wang, D. S. Wu, Y. G. Shi, and N. L. Wang, Anisotropic transport and optical spectroscopy study on antiferromagnetic triangular lattice EuCd$_2$As$_2$: An interplay between magnetism and charge transport properties, Phys. Rev. B **94**, 045112 (2016).

[45] G. Xu, H. Weng, Z. Wang, X. Dai, and Z. Fang, Chern semimetal and the quantized anomalous Hall effect in HgCr$_2$Se$_4$, Phys. Rev. Lett. **107**, 186806 (2011).

[46] J. Li, Y. Li, S. Du, Z. Wang, B.-L. Gu, S.-C. Zhang, K. He, W. Duan, and Y. Xu, Intrinsic magnetic topological insulators in van der Waals layered MnBi$_2$Te$_4$-family materials, Sci. Adv. **5**, eaaw5685 (2019).

[47] Y. Gao, W. Wu, B.-C. Gong, H.-C. Yang, X.-F. Zhou, Y. Liu, S. A. Yang, K. Liu, and Z.-Y. Lu, Intrinsic ferromagnetic axion states and single pair of Weyl fermions in the stable-state Mn$X_2B_2T_6$ family of materials, Phys. Rev. B **107**, 045136 (2023).

[48] J. A. Boulton and K. W. Kim, Search for an antiferromagnetic Weyl semimetal in (MnTe)$_m$(Sb$_2$Te$_3$)$_n$ and (MnTe)$_m$(Bi$_2$Te$_3$)$_n$ superlattices, J. Phys.: Condens. Matter **36**, 405601 (2024).

[49] H. Liu, J. Cao, Z. Zhang, J. Liang, L. Wang, and S. A. Yang, Ideal spin-polarized Weyl half-semimetal with a single pair of Weyl points in the half-Heusler compounds xCrTe (x = K, Rb), Phys. Rev. B **109**, 174426 (2024).

[50] A. B. Sushkov, J. B. Hofmann, G. S. Jenkins, J. Ishikawa, S. Nakatsuji, S. Das Sarma, and H. D. Drew, Optical evidence for a Weyl semimetal state in pyrochlore Eu$_2$Ir$_2$O$_7$, Phys. Rev. B **92**, 241108(R) (2015).

[51] Y. Cheon, M. T. Kiani, Y.-H. Tu, S. Kumar, N. K. Duong, J. Kim, Q. P. Sam, H. Wang, S. K. Kushwaha, N. Ng, S. H. Lee, S. Kielar, C. Li, D. Koumoulis, S. Siddique, Z. Mao, G. Jin, Z. Tian, R. Sundararaman, and H. Lin *et al.*, Surface-dominant transport in Weyl semimetal NbAs nanowires for next-generation interconnects, arXiv:2503.04621 [cond-mat.mes-hall].

[52] V. Kaladzhyan and J. H. Bardarson, Quantized Fermi arc mediated transport in Weyl semimetal nanowires, Phys. Rev. B **100**, 085424 (2019).

[53] P. O. Sukhachov, M. V. Rakov, O. M. Teslyk, and E. V. Gorbar, Fermi arcs and DC transport in nanowires of Dirac and Weyl semimetals, Ann. Phys. **532**, 1900449 (2020).

[54] A. De Martino, K. Dorn, F. Buccheri, and R. Egger, Phonon-induced magnetoresistivity of Weyl semimetal nanowires, Phys. Rev. B **104**, 155425 (2021).

[55] W. Duan, X. D. Lu, and J.-F. Liu, Large optical conductivity of Fermi arc states in Weyl and Dirac semimetal nanowires, Phys. Rev. B **108**, 195436 (2023).

[56] A. G. Grushin, Consequences of a condensed matter realization of Lorentz-violating QED in Weyl semi-metals, Phys. Rev. D **86**, 045001 (2012).

[57] A. Burkov, Weyl metals, Annu. Rev. Condens. Matter Phys. **9**, 359 (2018).

[58] N. P. Armitage and L. Wu, On the matter of topological insulators as magnetoelectrics, SciPost Phys. **6**, 046 (2019).

[59] A. A. Burkov, Anomalous Hall effect in Weyl metals, Phys. Rev. Lett. **113**, 187202 (2014).

[60] N. Ashcroft and N. Mermin, *Solid State Physics* (Thomson Learning, Inc., 1976).

[61] O. V. Kotov and Y. E. Lozovik, Dielectric response and novel electromagnetic modes in three-dimensional Dirac semimetal films, Phys. Rev. B **93**, 235417 (2016).

[62] G. Grosso and G. Parravicini, *Solid State Physics* (Elsevier Science, Amsterdam, 2000).

[63] C. A. Pfeiffer, E. N. Economou, and K. L. Ngai, Surface polaritons in a circularly cylindrical interface: Surface plasmons, Phys. Rev. B **10**, 3038 (1974).

[64] J. Stratton, *Electromagnetic Theory*, IEEE Press Series on Electromagnetic Wave Theory (John Wiley & Sons, Inc., New Jersey, 2007).

[65] K. Deng, J. S. Van Dyke, D. Minic, J. J. Heremans, and E. Barnes, Exploring self-consistency of the equations of axion

electrodynamics in Weyl semimetals, Phys. Rev. B **104**, 075202 (2021).

[66] S. A. Hassani Gangaraj, C. Valagiannopoulos, and F. Monticone, Topological scattering resonances at ultralow frequencies, Phys. Rev. Res. **2**, 023180 (2020).

[67] M. Schüler, U. De Giovannini, H. Hübener, A. Rubio, M. A. Sentef, and P. Werner, Local Berry curvature signatures in dichroic angle-resolved photoelectron spectroscopy from two-dimensional materials, Sci. Adv. **6**, eaay2730 (2020).

[68] M. Ünzelmann, H. Bentmann, T. Figgemeier, P. Eck, J. N. Neu, B. Geldiyev, F. Diekmann, S. Rohlf, J. Buck, M. Hoesch, M. Kalläne, K. Rossnagel, R. Thomale, T. Siegrist, G. Sangiovanni, D. Di Sante, and F. Reinert, Momentum-space signatures of Berry flux monopoles in the Weyl semimetal TaAs, Nat. Commun. **12**, 3650 (2021).

[69] Y. Yao, L. Kleinman, A. H. MacDonald, J. Sinova, T. Jungwirth, D.-S. Wang, E. Wang, and Q. Niu, First principles calculation of anomalous Hall conductivity in ferromagnetic bcc Fe, Phys. Rev. Lett. **92**, 037204 (2004).

[70] E. Liu, Y. Sun, N. Kumar, L. Muechler, A. Sun, L. Jiao, S.-Y. Yang, D. Liu, A. Liang, Q. Xu *et al.*, Giant anomalous Hall effect in a ferromagnetic kagome-lattice semimetal, Nat. Phys. **14**, 1125 (2018).

[71] M. Buchhold, S. Diehl, and A. Altland, Nodal points of Weyl semimetals survive the presence of moderate disorder, Phys. Rev. B **98**, 205134 (2018).

[72] F. Buccheri, A. De Martino, R. G. Pereira, P. W. Brouwer, and R. Egger, Phonon-limited transport and fermi arc lifetime in Weyl semimetals, Phys. Rev. B **105**, 085410 (2022).

[73] M. Hentschel, M. Schäferling, X. Duan, H. Giessen, and N. Liu, Chiral plasmonics, Sci. Adv. **3**, e1602735 (2017).

[74] Z. Jalali-Mola and S. A. Jafari, Electrodynamics of tilted Dirac and Weyl materials: A unique platform for unusual surface plasmon polaritons, Phys. Rev. B **100**, 205413 (2019).

[75] S. S.-L. Zhang and G. Vignale, Chiral surface and edge plasmons in ferromagnetic conductors, Phys. Rev. B **97**, 224408 (2018).

[76] K. Shastri, M. I. Abdelrahman, and F. Monticone, Nonreciprocal and topological plasmonics, Photonics **8**, 133 (2021).

[77] P. Genevet, J. Lin, M. A. Kats, and F. Capasso, Holographic detection of the orbital angular momentum of light with plasmonic photodiodes, Nat. Commun. **3**, 1278 (2012).

[78] H. Kim, J. Park, S.-W. Cho, S.-Y. Lee, M. Kang, and B. Lee, Synthesis and dynamic switching of surface plasmon

vortices with plasmonic vortex lens, Nano Lett. **10**, 529 (2010).

[79] B. A. Knyazev, Y. Y. Choporova, M. S. Mitkov, V. S. Pavelyev, and B. O. Volodkin, Generation of terahertz surface plasmon polaritons using nondiffractive Bessel beams with orbital angular momentum, Phys. Rev. Lett. **115**, 163901 (2015).

[80] D. E. Chang, A. S. Sørensen, P. R. Hemmer, and M. D. Lukin, Quantum optics with surface plasmons, Phys. Rev. Lett. **97**, 053002 (2006).

[81] M. I. Stockman, Nanofocusing of optical energy in tapered plasmonic waveguides, Phys. Rev. Lett. **93**, 137404 (2004).

[82] I. Aharonovich, D. Englund, and M. Toth, Solid-state single-photon emitters, Nat. Photon. **10**, 631 (2016).

[83] B. Chen, Y. Wei, T. Zhao, S. Liu, R. Su, B. Yao, Y. Yu, J. Liu, and X. Wang, Bright solid-state sources for single photons with orbital angular momentum, Nat. Nanotechnol. **16**, 302 (2021).

[84] W. Jiang, Q. Zhou, J. He, M. A. Habibi, S. Melnyk, M. El-Absi, B. Han, M. D. Renzo, H. D. Schotten, F.-L. Luo, T. S. El-Bawab, M. Juntti, M. Debbah, and V. C. M. Leung, Terahertz communications and sensing for 6g and beyond: A comprehensive review, IEEE Commun. Surv. Tutor. **26**, 2326 (2024).

[85] A. Tredicucci and M. S. Vitiello, Infrared and terahertz quantum technologies, Nanophotonics **13**, 1677 (2024).

[86] S. Yuan, L. Chen, Z. Wang, W. Deng, Z. Hou, C. Zhang, Y. Yu, X. Wu, and X. Zhang, On-chip terahertz isolator with ultrahigh isolation ratios, Nat. Commun. **12**, 5570 (2021).

[87] M. Peluso, A. De Martino, R. Egger, and F. Buccheri, Dataset on Zenodo (2025), accompanying dataset for Figs. 2, 3, 4.

[88] D. C. Langreth, Macroscopic approach to the theory of reflectivity, Phys. Rev. B **39**, 10020 (1989).

[89] L. Landau, E. M. Lifshitz, and L. P. Pitaevskii, *Electrodynamics of Continuous Media*, 2nd ed. (Elsevier Butterworth-Heinemann, Oxford, 2006).

[90] DLMF, NIST Digital Library of Mathematical Functions, https://dlmf.nist.gov/, Release 1.2.1 of 2024-06-15, edited by F. W. J. Olver, A. B. Olde Daalhuis, D. W. Lozier, B. I. Schneider, R. F. Boisvert, C. W. Clark, B. R. Miller, B. V. Saunders, H. S. Cohl, and M. A. McClain.

[91] D. Santos-Cottin, I. Mohelský, J. Wyzula, F. Le Mardelé, I. Kapon, S. Nasrallah, N. Barišić, I. Živković, J. R. Soh, F. Guo, K. Rigaux, M. Puppin, J. H. Dil, B. Gudac, Z. Rukelj, M. Novak, A. B. Kuzmenko, C. C. Homes, T. Dietl, and M. Orlita *et al.*, EuCd$_2$As$_2$: A Magnetic Semiconductor, Phys. Rev. Lett. **131**, 186704 (2023).